Equation of state of dense plasmas with pseudoatom molecular dynamics

C. E. Starrett and D. Saumon

Phys. Rev. E **93**, 063206 — Published 14 June 2016

DOI: 10.1103/PhysRevE.93.063206

Equation of state of dense plasmas with pseudoatom molecular dynamics

C. E. Starrett[1,*] and D. Saumon[1]

[1]*Los Alamos National Laboratory, P.O. Box 1663, Los Alamos, NM 87545, U.S.A.*

(Dated: May 31, 2016)

We present an approximation for calculating the equation of state (EOS) of warm and hot dense matter that is built on the previously published Pseudoatom Molecular Dynamics (PAMD) model of dense plasmas [Starrett *et al.*, Phys. Rev. E **91**, 013104 (2015)]. While the EOS calculation with PAMD was previously limited to orbital-free density functional theory (DFT), the new approximation presented here allows a Kohn-Sham DFT treatment of the electrons. The resulting EOS thus includes a quantum mechanical treatment of the electrons with a self-consistent model of the ionic structure, while remaining tractable at high temperatures. The method is validated by comparisons with pressures from ab initio simulations of Be, Al, Si and Fe. The EOS in the Thomas-Fermi approximation shows remarkable thermodynamic consistency over a wide range of temperature for aluminum. We calculate the principal Hugoniots of aluminum and silicon up to 500 eV. We find that the ionic structure of the plasma has a modest effect that peaks at temperatures of a few eV and that the features arising from the electronic structure agree well with ab initio simulations.

PACS numbers: 52.25.Kn, 52.27.Gr, 52.65.Yy

I. INTRODUCTION

In the interiors of giant planets, the envelopes of white dwarf stars and in inertial confinement fusion experiments, material conditions referred to as warm and hot dense matter are encountered [1–3]. Such conditions are characterized by electron-electron, ion-electron and ion-ion correlations of comparable importance. Atoms in these plasmas are partially ionized and the ionic fluid can range from strongly to weakly coupled. A self-consistent treatment of all these physical effects is therefore challenging.

For relatively low temperatures the method of choice for simulating warm dense matter is Kohn-Sham (KS) density functional theory molecular dynamics (DFT-MD)[1] [4]. While this method is thought to be accurate for equation of state (EOS) calculations, it quickly becomes prohibitively expensive with increasing temperatures [5]. The computational cost of Orbital-Free DFT-MD [6] [2] has a more manageable temperature scaling at the cost of physical accuracy, but it remains expensive. A modified version of the high-temperature method of Path Integral Monte Carlo (PIMC) has enabled its application to elements beyond helium [7]; currently up to silicon [8].

Recently [9] we have developed a new method for modeling the properties of warm and hot dense matter that we call pseudoatom molecular dynamics (PAMD). This can be characterized as an approximate version of Kohn-Sham or orbital free molecular dynamics (both versions of PAMD have been developed) that combines an average atom model of the electronic structure with molecular dynamics for the ionic structure. In the Thomas-Fermi orbital free version, the equation of state and the self-diffusion coefficient are of an accuracy comparable to the corresponding OFMD simulations [9]. In this paper we describe the formulation of the thermodynamics of PAMD. We evaluate the thermodynamic consistency of the PAMD-TF method and show that it is remarkably consistent for a wide range of temperatures for an aluminum plasma. We then develop and validate an approximation for equation of state calculations with the Kohn-Sham version of PAMD, finding good to excellent agreement with QMD and Path Integral Monte Carlo (PIMC) simulations. We compare the pressures from PAMD (both Kohn-Sham and Orbital Free) to corresponding average atom models, showing the influence of a self-consistent treatment of ionic structure. We also directly compare pressures from Kohn-Sham and orbital free PAMD. Finally we use PAMD to calculate the principal Hugoniots of aluminum up to 500 eV, and of silicon up to 1 keV, far beyond the temperature range accessible to QMD simulations. Unless otherwise stated we use Hartree atomic units in which $\hbar = m_e = e = 1$, where the symbols have their usual meaning.

II. THERMODYNAMICS WITH PSEUDOATOM MOLECULAR DYNAMICS

A. Summary of the Pseudoatom Molecular Dynamics model

Central to PAMD is the superposition approximation for the total electron density. We assume that the plasma

*Electronic address: starrett@lanl.gov

[1] Here we refer to KS-DFT-MD as quantum molecular dynamics (QMD).

[2] We refer to OF-DFT-MD simply as OFMD.

is an ensemble of identical pseudoatoms[3] that are constructed numerically by solving an average atom model [11, 12]. On the basis of the superposition approximation, one can show that by using the pseudoatom electron density as a closure relation for the quantum Ornstein-Zernike equations, an effective ionic pair interaction potential can be uniquely determined [11]. This potential can be used in the Ornstein-Zernike equation to solve for the static ionic structure. Alternatively the same potential can be used in classical molecular dynamics simulations [9] which allows the calculation of dynamical ion properties (also see [13, 14]) as well as the equation of state of the plasma.

The physical motivation for expecting the plasma electron density to be reasonably represented by an ensemble of identical pseudoatoms is based on to two observations. The first is that for deeply bound electrons the separation into pseudoatoms is clearly accurate. For continuum electrons, the separation is exact in the linear response regime [12]. The combination of these observations suggests that the pseudoatom approximation is reasonable, and becomes exact where continuum electrons respond linearly to the ionic potential. This is borne out by extensive validation of the model (see below).

Each pseudoatom has a nuclear charge Z and electron density $n_{\rm e}^{\rm PA}(r)$, where

$$\int d^3r\, n_{\rm e}^{\rm PA}(r) = Z. \tag{1}$$

The electron density of the (infinite) plasma is then

$$n_{\rm e}(\boldsymbol{r}) = \sum_{i=1}^{\infty} n_{\rm e}^{\rm PA}(|\boldsymbol{R}_i - \boldsymbol{r}|) \tag{2}$$

where $\{\boldsymbol{R}_i\}$ is the set of position vectors of the nuclei. For all the calculations in this paper we use $n_{\rm e}^{\rm PA}(r)$ as generated by the ion-sphere average atom model presented in [12]. The average atom model is based on density functional theory. Both orbital free (here we use the Thomas-Fermi (PAMD-TF) approximation) and Kohn-Sham (PAMD-KS) treatments of the electrons have been developed. The nuclear positions $\{\boldsymbol{R}_i\}$ are generated with classical molecular dynamics [9]. The pseudoatom pair interaction potential $V(r)$ that is input to the molecular dynamics simulations is generated from $n_{\rm e}^{\rm PA}(r)$. Once the contribution of the valence electrons to $n_{\rm e}^{\rm PA}(r)$ has been defined as $n_{\rm e}^{\rm scr}(k)$ [12], the potential $V(r)$ is given by (in Fourier space)

$$V(k) = \frac{4\pi}{k^2}\bar{Z}^2 + \frac{\left(n_{\rm e}^{\rm scr}(k)\right)^2}{\chi_{\rm e}(k)}, \tag{3}$$

where $\bar{Z} = \int d^3r\, n_{\rm e}^{\rm scr}(r)$ is the ion charge and $\chi_{\rm e}(k)$ is the response function of the electrons (see equation (17) of [12]). The potential $V(r)$ has no assumed functional form or adjustable parameters and is easily calculated once $n_{\rm e}^{\rm PA}(r)$ is determined.

The PAMD model contains unconstrained approximations whose limit of validity in terms of the physical parameters of the system is a priori unknown. To establish the range of applicability of the model, we have carried out a large amount of validation in the warm and hot dense matter regimes, primarily by comparison with ab initio simulations. In the interest of brevity, we simply list these comparisons below, noting that in every case the agreement is very good to excellent unless otherwise indicated. In reference [11], where the pseudoatom model was first introduced, ion-ion pair distribution functions were presented for hydrogen, aluminum, and iron, and for the high-Z element tungsten in [12]. In reference [10] the model was extended to mixtures, with a study of the ion-ion pair distribution functions of carbon/hydrogen mixtures in both the Thomas-Fermi and Kohn-Sham models of the electrons. In the latter case, we found poor agreement with simulations at temperatures below a few eV and solid density where C-C bonds appear in the simulations, a phenomenon that is not captured by the PAMD model. In [15] the X-ray elastic scattering feature, which is closely related to the ion structure factor, is compared to an accurate experimental measurement of warm dense aluminum [16]. The introduction of molecular dynamics for the ions in PAMD allowed the calculation of the equation of state, ionic diffusion coefficients and viscosity with PAMD, with applications to aluminum and a iron/helium mixture (EOS), and hydrogen, deuterium, boron, aluminum, iron, copper (self-diffusion) [9, 13].

This extensive validation has shown that PAMD becomes inaccurate in the solid or liquid regimes (i.e. normal densities and temperatures below 1 eV), but is accurate at these densities and higher, at temperatures such that the ion fluid is not too strongly coupled (i.e. effective ion-ion coupling parameter [17] $\Gamma_{\rm eff} \lesssim 55$). On the basis of the physical underpinning of the model, the inability of the pseudoatom model to model bonds is obvious, while the breakdown at very low temperatures is likely due to the inaccurate treatment of long range Friedel oscillations that occur when free electrons are strongly degenerate (see below). The method has not been developed to model lower density plasmas, since in the current implementation the ion-ion interaction is mediated by the ionized electrons, and at low densities and temperatures the ionization fraction can become very small, leading to an unreliable ion-ion potential. The present contribution extends the model's capability to the calculation of the EOS with the Kohn-Sham model of the electrons.

[3] For plasma mixtures there are different pseudoatoms for each species [10].

B. Thermodynamics in the superposition approximation

The electrostatic energy of a plasma can be written

$$E^{\mathrm{el}} = E_{\mathrm{ii}} + E_{\mathrm{ie}} + E_{\mathrm{ee}} \tag{4}$$

where

$$E_{\mathrm{ii}} = \frac{1}{2}\sum_{i=1}^{\infty}\sum_{\substack{j=1\\ j\neq i}}^{\infty}\frac{Z^2}{|\boldsymbol{R}_i - \boldsymbol{R}_j|} \tag{5}$$

$$E_{\mathrm{ie}} = -\sum_{j=1}^{\infty}\int d^3r\,\frac{Z n_{\mathrm{e}}(\boldsymbol{r})}{|\boldsymbol{R}_j - \boldsymbol{r}|} \tag{6}$$

$$E_{\mathrm{ee}} = \frac{1}{2}\int d^3r \int d^3r'\,\frac{n_{\mathrm{e}}(\boldsymbol{r}) n_{\mathrm{e}}(\boldsymbol{r}')}{|\boldsymbol{r}' - \boldsymbol{r}|} \tag{7}$$

Using the superposition approximation (Eq. (2)), equations (5) to (7) can be written for a subset of N pseudoatoms in a periodically repeating cell

$$E_{\mathrm{ii}} = \frac{1}{2}\sum_{i=1}^{N}\sum_{\substack{j=1\\ j\neq i}}^{\infty}\frac{Z^2}{|\boldsymbol{R}_i - \boldsymbol{R}_j|} \tag{8}$$

$$E_{\mathrm{ie}} = -\sum_{i=1}^{N}\sum_{j=1}^{\infty}\int d^3r\,\frac{Z n_{\mathrm{e}}^{\mathrm{PA}}(|\boldsymbol{R}_j - \boldsymbol{r}|)}{|\boldsymbol{R}_i - \boldsymbol{r}|} \tag{9}$$

$$E_{\mathrm{ee}} = \frac{1}{2}\sum_{i=1}^{N}\sum_{j=1}^{\infty}\int d^3r \int d^3r'\,\frac{n_{\mathrm{e}}^{\mathrm{PA}}(|\boldsymbol{R}_i - \boldsymbol{r}|) n_{\mathrm{e}}^{\mathrm{PA}}(|\boldsymbol{R}_j - \boldsymbol{r}'|)}{|\boldsymbol{r}' - \boldsymbol{r}|} \tag{10}$$

On combining equations (8) to (10) the electrostatic energy separates into a term that does not explicitly depend on the ionic structure (the non-structural term E^{NS}) and a term that does (the structural term E^{S})

$$E^{\mathrm{el}} = E^{\mathrm{NS}} + E^{\mathrm{S}} \tag{11}$$

where

$$E^{\mathrm{NS}} = \frac{N}{2}\int d^3r\, n_{\mathrm{e}}^{\mathrm{PA}}(r)\left[\frac{-Z}{r} + V^{\mathrm{PA}}(r)\right] \tag{12}$$

and

$$\begin{aligned} E^{\mathrm{S}} \;=\; & \frac{1}{2}\sum_{i=1}^{N}\sum_{\substack{j=1\\ j\neq i}}^{\infty}\{-ZV^{\mathrm{PA}}(|\boldsymbol{R}_i - \boldsymbol{R}_j|) \\ & + \mathcal{F}^{-1}\left[\tilde{n}_{\mathrm{e}}^{\mathrm{PA}}(k)\tilde{V}^{\mathrm{PA}}(k)\right](|\boldsymbol{R}_i - \boldsymbol{R}_j|)\Big\} \end{aligned} \tag{13}$$

where

$$V^{\mathrm{PA}}(r) \equiv \frac{-Z}{r} + \int d^3r'\,\frac{n_{\mathrm{e}}^{\mathrm{PA}}(r')}{|\boldsymbol{r}' - \boldsymbol{r}|}, \tag{14}$$

the tilde indicates a Fourier transformed function and $\mathcal{F}^{-1}$ is the inverse Fourier transform operator. This form of E^{el} (equations 11–13) is suitable for evaluation with molecular dynamics.

The structural term (Eq. (13)) can be further simplified as follows. The Fourier transform of the microscopic density $\rho_{\boldsymbol{k}}$ is defined as [18]

$$\rho_{\boldsymbol{k}} = \sum_{i=1}^{N} e^{-\imath \boldsymbol{k}\cdot\boldsymbol{R}_i} \tag{15}$$

and its relation to the ionic structure factor [18] is

$$S_{\mathrm{ii}}(k) = \frac{1}{N}\langle \rho_{\boldsymbol{k}}\rho_{-\boldsymbol{k}}\rangle \tag{16}$$

where the angular brackets indicate that the configurational average has been taken. Using Eqs. (15) and (16), E^S can be written in terms of the ionic structure factor. Since [18]

$$S_{\mathrm{ii}}(k) = 1 + n_{\mathrm{I}}^0(2\pi)^3\delta(\boldsymbol{k}) + n_{\mathrm{I}}^0 h_{\mathrm{ii}}(k), \tag{17}$$

where n_{I}^0 is the particle density of the nuclei, $h_{\mathrm{ii}}(k)$ the pair correlation function, and $\delta(\boldsymbol{k})$ the δ-function, the configurational average of the structural contribution becomes

$$\left\langle E^{\mathrm{S}}\right\rangle = \frac{N}{2}\left(-ZV_{\mathrm{Ne}}^{\mathrm{ext}}(r=0) + \int d^3r\, n_{\mathrm{e}}^{\mathrm{PA}}(r)V_{\mathrm{Ne}}^{\mathrm{ext}}(r)\right) \tag{18}$$

where

$$V_{\mathrm{Ne}}^{\mathrm{ext}}(r) \equiv n_I^0\int d^3r'\, g_{\mathrm{ii}}(|\boldsymbol{r}' - \boldsymbol{r}|)V^{\mathrm{PA}}(r') \tag{19}$$

Therefore, with knowledge of the pseudoatom electron density $n_{\mathrm{e}}^{\mathrm{PA}}(r)$ and the ionic structure factor (or equivalently the pair distribution function $g_{\mathrm{ii}}(r) = h_{\mathrm{ii}}(r) + 1$), the electrostatic free energy

$$F^{\mathrm{el}} = E^{\mathrm{NS}} + \left\langle E^{\mathrm{S}}\right\rangle \tag{20}$$

can be calculated without further approximation. If $g_{\mathrm{ii}}(r)$ is determined using the Ornstein-Zernike equations as in reference [12], then Eqs. (12) and (18) are used. For MD simulations we use equation (13) for the structural term, averaged over a number of ionic configurations to get $\left\langle E^{\mathrm{S}}\right\rangle$.

In the Thomas-Fermi (TF) approximation the kinetic energy of the electrons in a plasma of volume V containing N nuclei can be written

$$K_e^{\mathrm{TF}} = \frac{1}{\beta}\int_V d^3r\, c_{\mathrm{TF}} I_{3/2}\left[\eta(\boldsymbol{r})\right)] \tag{21}$$

and the free energy is given by

$$F^{\mathrm{TF}} = \frac{1}{\beta}\int_V d^3r\,\left(n_{\mathrm{e}}(\boldsymbol{r})\eta(\boldsymbol{r}) - \frac{2}{3}c_{\mathrm{TF}} I_{3/2}\left[\eta(\boldsymbol{r})\right)]\right) \tag{22}$$

where $\beta = 1/T$ is the inverse temperature, I_j is the Fermi integral of order j (see [11]) and

$$c_{\rm TF} \equiv \frac{\sqrt{2}}{\pi^2 \beta^{3/2}}. \tag{23}$$

The electron density in this approximation is

$$n_{\rm e}(\boldsymbol{r}) = c_{TF} I_{1/2}\left[\eta(\boldsymbol{r})\right)] \tag{24}$$

Given the electron density in the superposition approximation (Eq. (2)), the function $\eta(\boldsymbol{r})$ is obtained by inverting equation (24) which can then be substituted into equations (21) and (22). An important point to realize here is that the electron density $n_{\rm e}(\boldsymbol{r})$ in equation (2) cannot be obtained from $n_{\rm e}^{\rm PA}(r)$ and $g_{\rm ii}(r)$ without further approximation and therefore cannot be directly calculated from the model presented in [11, 12]. In turn, while F^{el} can be calculated from $n_{\rm e}^{\rm PA}(r)$ and $g_{\rm ii}(r)$, F^{TF} and the exchange-correlation free energy $F_{\rm ee}^{\rm xc}$ (see below), cannot. One must have access to the set of ionic positions $\{\boldsymbol{R}_i\}$ to allow construction of the electron density $n_{\rm e}(\boldsymbol{r})$ via Eq. (2). Fortunately $\{\boldsymbol{R}_i\}$ can be generated using classical MD. This makes it possible to calculate the other components of the total free energy for a given MD snapshot. The configurational average can then be generated in the usual way by averaging MD snapshots under the ergodic hypothesis [19].

The free energy of the electron exchange and correlation energy is handled in a similar way. In the local density approximation (LDA),

$$F_{\rm ee}^{\rm xc} = \int_V d^3r\, f_{\rm ee}^{\rm xc}\left[n_{\rm e}(\boldsymbol{r})\right], \tag{25}$$

which can be calculated directly from $n_{\rm e}^{\rm PA}(r)$ and $\{\boldsymbol{R}_i\}$.

The total the free energy is given by

$$F = F^{\rm TF} + F^{\rm I} + F^{\rm el} + F_{\rm ee}^{\rm xc}. \tag{26}$$

where F^I is the free energy of an ideal gas of ions. The internal energy per atom is

$$U = \frac{1}{N}(K_{\rm e}^{\rm TF} + K^{\rm I} + F^{\rm el} + U^{\rm xc}) \tag{27}$$

where $U^{\rm xc}$ is the contribution to the internal energy from exchange and correlations

$$U^{\rm xc} = F_{\rm ee}^{\rm xc} - T\frac{\partial F_{\rm ee}^{\rm xc}}{\partial T} \tag{28}$$

and $K^{\rm I}$ is the ion kinetic energy

$$K^{\rm I} = \frac{3}{2} N\, T. \tag{29}$$

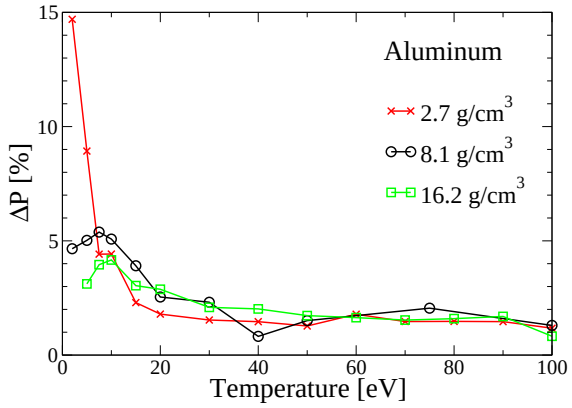

FIG. 1: Percent difference in the virial and thermodynamic pressures (see text) for aluminum. A positive difference indicates that $P^{\rm th} > P^{\rm vir}$. This is a stringent test of the accuracy of the superposition approximation (equation 2). In the limit of perfect physical and numerical accuracy the difference would be zero.

C. Calculation of the pressure

To calculate the pressure we use the Virial theorem, which can be derived [20–22] by assuming that the superposition approximation Eq. (2) is exact. The expression to evaluate is

$$P^{\rm vir}\, V = \frac{2}{3}K_{\rm e}^{\rm TF} + \frac{2}{3}K^{\rm I} + \frac{1}{3}F^{\rm el} + C^{\rm xc} \tag{30}$$

and $C^{\rm xc}$ is the contribution from exchange and correlation,

$$C^{\rm xc} = -F_{\rm ee}^{\rm xc} + \int_V d^3r\, n_{\rm e}(\boldsymbol{r})\frac{\delta F_{\rm ee}^{\rm xc}}{\delta n_{\rm e}(\boldsymbol{r})}. \tag{31}$$

An alternative route to calculate the pressure (which we call the thermodynamic pressure $P^{\rm th}$) is to take a numerical derivative of the free energy F with respect to the volume V

$$P^{\rm th} = -\left.\frac{\partial F}{\partial V}\right|_T. \tag{32}$$

$P^{\rm vir}$ and $P^{\rm th}$ are identical if the calculated $n_{\rm e}(\boldsymbol{r})$ minimizes the free energy [23, 24]. In PAMD $n_{\rm e}(\boldsymbol{r})$ is given by the superposition approximation, not by the minimization of the free energy. A comparison of the two pressures offers a internal check of the accuracy of this approximation. In figure 1 we compare $P^{\rm vir}$ and $P^{\rm th}$ for aluminum as a function of temperature. The virial pressure $P^{\rm vir}$ (equation (30)) converges quickly with respect to number of particles and time steps. For $P^{\rm th}$ we found it necessary to use rather large MD simulations (40 000 particles) to perform accurate numerical differentiation of the free energy. For the higher temperatures it was also necessary to extend the length of the simulations to 20 000 time steps. Even so, some numerical

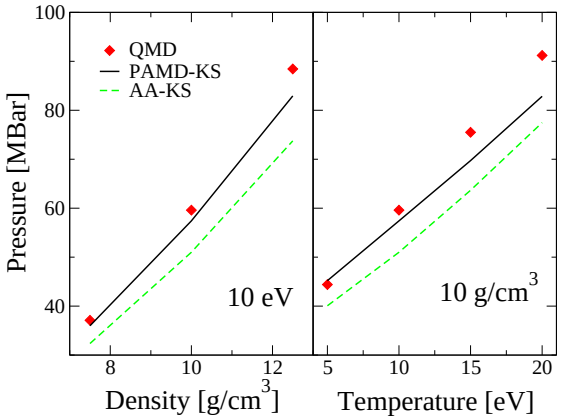

FIG. 2: Pressures from PAMD-KS compared to QMD [26] for beryllium. Also shown are pressures from an average atom model (AA-KS). PAMD-KS agrees significantly better with the QMD calculations.

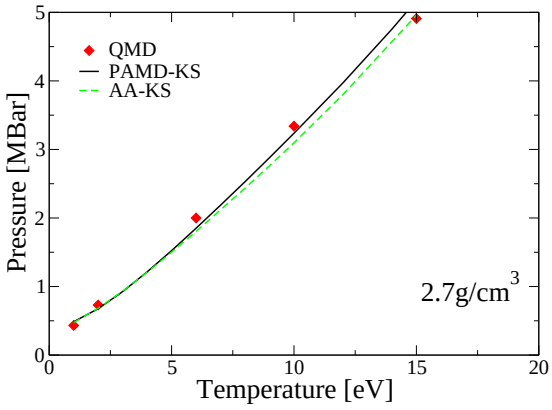

FIG. 3: Pressures from PAMD-KS compared to QMD [27] for aluminum. Also shown are pressures from an average atom model (AA-KS). Both PAMD-KS and AA-KS agree well with the QMD calculations.

T [eV]	ρ [g/cm^3]	QMD	PAMD-KS	TFMD	PAMD-TF
5	18.71	16.1	15.60		25.64
10	22.5	32.4	36.72	51.3	48.25
100	34.5		663.6	683.3	672.8
1000	39.65		14568	14765	14818

TABLE I: A comparison of total pressure (Mbar) for iron between PAMD and corresponding DFT-MD simulations [27, 28] for a range of temperatures (T) and densities (ρ).

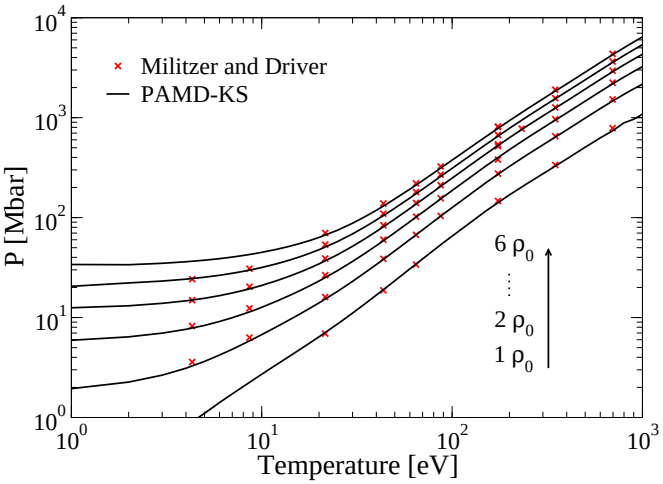

FIG. 4: Isochores of the total pressure for silicon from PAMD-KS compared to the QMD/PIMC results of Militzer and Driver [8]. The isochores shown are in multiples of the normal solid density of $\rho_0 = 2.33\,\mathrm{g/cm^3}$, from ρ_0 (bottom) to $6\rho_0$ (top). The differences remain below 9% everywhere and a generally below 5%.

noise persists in P^{th} at the 1% level. For the higher temperatures shown the relative difference in the pressures is $2-3\%$. This represents a very stringent test on the numerics of the implementation. For lower temperatures we see larger differences, approaching $\sim 15\%$ at 2 eV and 2.7 $\mathrm{g\,cm^{-3}}$. This indicates that the superposition approximation becomes poorer at these lower temperatures and density, though still quite reasonable. This deviation from thermodynamic consistency is similar to the trend caused by the variational inconsistency of two Kohn-Sham AA models (INFERNO [25], and a neutral Wigner-Seitz (NWS) sphere atom-in-jellium model), as discussed in ref. [22]. In the latter two models, the inconsistency is attributed to the handling of the long-range Friedel oscillations that occur in the electron density at low temperatures. The error in thermodynamic consistency of the PAMD model (figure 1) likely arises from the linear superposition of the Friedel oscillations being a poor approximation to the actual effect [4]. In summary, the superposition approximation is accurate over a wide range of temperatures, which validates this core assumption of the PAMD model.

[4] For an example of Friedel oscillations in the pseudoatom electron density see figure 1 of reference [9].

D. Numerical evaluation of the free energy

Given the set of ion positions $\{\boldsymbol{R}_i\}$ from MD, the electrostatic energy E^{el} is evaluated directly using equations (11–13). In general the magnitude of the non-structural term (equation (12)) dominates that of the structural term. However both terms must be accurately evaluated for pressure calculations.

To numerically evaluate the volume integrals for the kinetic and exchange and correlation energies (equations

(21) and (25)) one could discretize the simulation volume with a non-uniform grid that allows an accurate integration for a given set of $\{\boldsymbol{R}_i\}$. However, the divergence of the TF electron density as $r^{-3/2}$ near each nuclear site[5] presents a numerical difficulty. This can be circumvented with a computational trick. Using the kinetic free energy (Eq. 21) as an example, we define a pseudoatom kinetic energy density $k_{\rm e}^{\rm TF,PA}(r)$:

$$k_{\rm e}^{\rm TF,PA}(r) \equiv k_{\rm e}^{\rm TF,full}(r) - k_e^{\rm TF,ext}(r) \tag{33}$$

where

$$k_{\rm e}^{TF,full}(r) \equiv \frac{1}{\beta} c_{\rm TF} I_{3/2}\left[\beta(\mu_{\rm e}^{\rm id} - V_{\rm Ne}^{\rm eff}(r))\right] \tag{34}$$

and

$$k_{\rm e}^{\rm TF,ext}(r) \equiv \frac{1}{\beta} c_{\rm TF} I_{3/2}\left[\beta(\mu_{\rm e}^{\rm id} - V_{\rm e}^{\rm eff,ext}(r))\right] \tag{35}$$

The terms in these equations are defined in equations (4) and (7) of Ref. [12]. This definition of $k_e^{TF,PA}$ is the analogue of the definition of the pseudoatom electron density $n_{\rm e}^{\rm PA}(r)$ (equation (8) of ref. [12]). We then construct the kinetic energy density in the superposition approximation (in analogy with Eq. (2))

$$k_{\rm e}^{\rm TF,super}(\boldsymbol{r}) = \sum_{i=1}^{\infty} k_{\rm e}^{\rm TF,PA}(|\boldsymbol{R}_i - \boldsymbol{r}|) \tag{36}$$

Numerically we then calculate the kinetic energy (Eq. (21)) in the form

$$K_{\rm e}^{\rm TF} = K_{\rm e}^{\rm TF,S} + N\, K_{\rm e}^{\rm TF,PA} \tag{37}$$

where

$$K_{\rm e}^{\rm TF,S} = \int_V d^3r \left(\frac{1}{\beta} c_{\rm TF} I_{3/2}\left[\eta(\boldsymbol{r})\right] - k_{\rm e}^{\rm TF,super}(\boldsymbol{r})\right) \tag{38}$$

and

$$K_e^{\rm TF,PA} \equiv \int d^3r\, k_e^{\rm TF,PA}(r). \tag{39}$$

Equations (37) to (39) give an exact representation of K_e^{TF}. The integral in equation (39) can be rapidly evaluated on a non-uniform grid and only needs to be carried out once for a given equation of state point. The integrand in Eq. (38) is slowly varying as the singularities have been removed; it can be evaluated efficiently on a uniformly spaced grid. $K_e^{TF,S}$ is generally small in magnitude relative to the $N\,K_e^{\rm TF,PA}$ term, but nevertheless cannot be ignored for pressure calculations. The other volume integrals can be evaluated in the same way. We note here that the same trick could be used in OFMD simulations, obviating the need for a pseudo-potential and allowing all-electron simulations.

[5] In Cartesian coordinates, the integrand for the kinetic energy integral diverges as $r^{-5/2}$ near nuclear sites.

E. An approximation for thermodynamics with the Kohn-Sham functional

As explained in [9], equations (30) and (27) can also be used in Kohn-Sham (KS) calculations if $K_e^{\rm TF}$ is replaced by the KS quantity $K_e^{\rm KS}$. However, to evaluate $K_e^{\rm KS}$ one needs not the electron density (as in the Thomas-Fermi case) but rather the multi-center electronic wavefunctions which are not provided by PAMD. Nevertheless, we can develop an approximate method based on the discussion of the previous section.

In analogy with equation (33) we define a KS pseudoatom kinetic energy density

$$k_e^{\rm KS,PA}(r) \equiv k_{\rm e}^{\rm KS,full}(r) - k_{\rm e}^{\rm KS,ext}(r) \tag{40}$$

where

$$k_{\rm e}^{\rm KS,full}(r) \equiv \int_{-\infty}^{\infty} d\epsilon\, g_\epsilon\, \epsilon\, \chi^{\rm full}(\epsilon, r) - n_{\rm e}^{\rm full}(r) V_{\rm Ne}^{\rm eff}(r) \tag{41}$$

and

$$\chi^{\rm full}(\epsilon, r) \equiv \sum_{l=0}^{\infty} \frac{2(2l+1)}{4\pi} \left|\frac{y_{\epsilon,l}(r)}{r}\right|^2 \tag{42}$$

and similarly for $k_{\rm e}^{\rm KS,ext}(r)$. An explanation of the terms in these equations is provided in appendix A of reference [12]. Defining

$$k_{\rm e}^{\rm KS,super}(\boldsymbol{r}) = \sum_{i=1}^{\infty} k_{\rm e}^{\rm KS,PA}(|\boldsymbol{R}_i - \boldsymbol{r}|) \tag{43}$$

we can then approximate $K_{\rm e}^{\rm KS}$ as

$$K_{\rm e}^{\rm KS} \approx K_{\rm e}^{\rm TF,S} + N\, K_{\rm e}^{\rm KS,PA} \tag{44}$$

where

$$K_{\rm e}^{\rm KS,PA} = \int_V d^3r\, k_{\rm e}^{\rm KS,PA}(r) \tag{45}$$

Whereas in the TF case equation (44) is just a numerical trick (see equation (37)), here it is actually a physical approximation: In the regions where $k_e^{KS,super}(r)$ is significantly different from the full orbital-based value, the electron kinetic energy density is approximated by the TF model. This is reasonable since for electrons moving in a constant potential the KS and TF treatments are identical, and the physical regions where such a differences exists are the interstitial regions (i.e. not near the nuclei), where the potential is relatively weak and slowly varying.

In figures 2–3 we compare PAMD results for pressure using this approximation for the Kohn-Sham functional (PAMD-KS) to QMD results [26]. We also plot the pressure from KS-based AA atom calculations (see the appendix). For beryllium PAMD-KS (figure 2) improves the agreement with the QMD data relative to the AA model, though differences up to $\sim 10\%$ remain at high

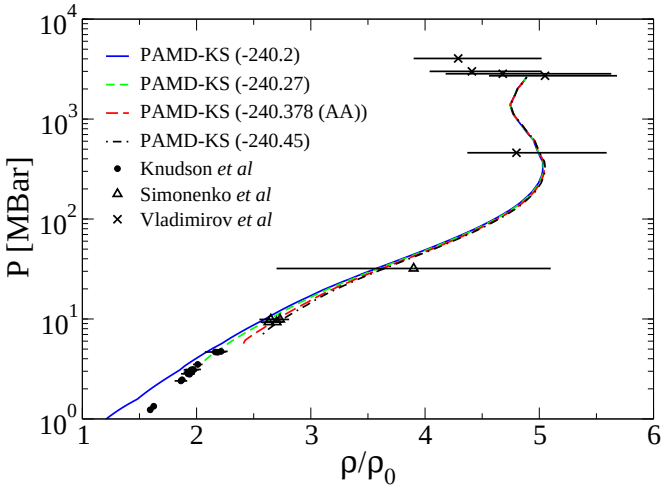

FIG. 5: Principal Hugoniot of aluminum from the PAMD-KS model for different choices of the initial internal energy U_0 (indicated in parentheses) in Hartree. The curve labeled "AA" uses the initial internal energy calculated using the KS average atom model. The experimental data are from refs. [29–31]. The Hugoniot is shown as a function of the compression ratio ρ/ρ_0 where $\rho_0 = 2.7$ g/cm^3 is the initial density. All PAMD curves cover a temperature range of 1 to 500 eV. The structure seen at high compression ratios is caused by the electronic shell structure of the bound states of Al.

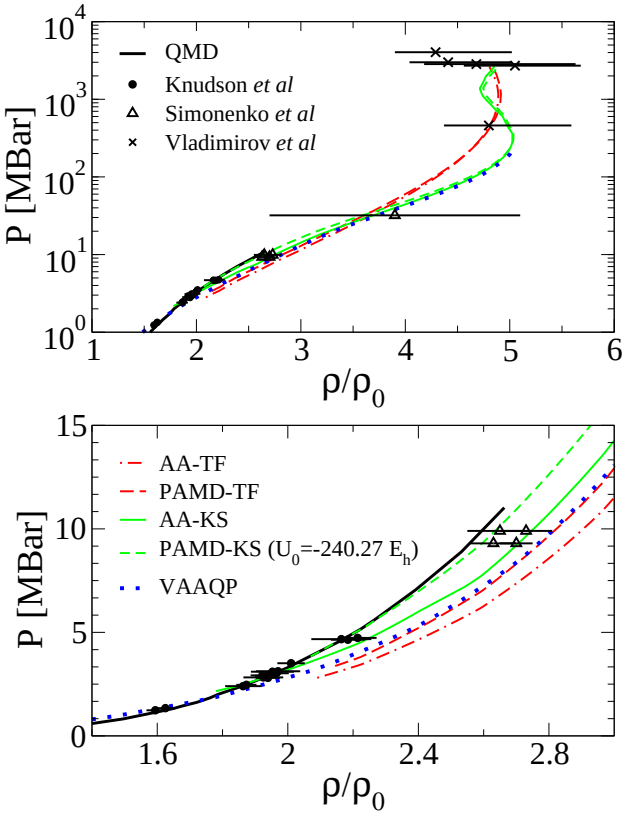

FIG. 6: Principal Hugoniot of aluminum from several models. The experimental data are from refs. [29–31]. The range of temperatures for the calculated Hugoniots is 1–500 eV. The QMD Hugoniot is from [32]. The top panel shows the full range of compression ration ρ/ρ_0, while the lower panel focuses on the smaller compression region only. Results from the VAAQP [22] model are also shown. The initial density is $\rho_0 = 2.7$ g/cm^3.

temperatures and densities. For aluminum (figure 3) both AA and PAMD give similar pressures, and both agree quite well with the QMD results.

By combining QMD simulations at low temperatures and PIMC simulations at high temperatures, it has recently been possible to generate a wide-ranging ab initio EOS table for silicon [8] that covers temperatures from 4.3 eV to 11.2 keV. A comparison of pressure isochores with our PAMD-KS calculation is shown in Figure 4. The agreement is excellent over the full temperature and density range shown. The differences in pressure generally remain below 5% and at worst reach 9%.

In table I we compare QMD, OFMD in the TF approximation (TFMD) to PAMD-KS and PAMD-TF results for iron. For the higher temperatures PAMD-TF and PAMD-KS give similar results for the pressure. For the lower temperatures the QMD and TFMD results differ significantly. PAMD-KS tracks the QMD result nicely, while PAMD-TF agrees well with the TFMD calculation. This demonstrates that our approximation to the KS kinetic energy (equation (44)) does not mask the KS character of the calculation.

F. Hugoniot calculations

In this section we use the PAMD model to assess the impact of a self-consistent treatment of ionic correlations on calculated shock compression curves. Given an equation of state, the Hugoniot is the solution to the Rankine-Hugoniot jump condition across the shock front

$$U - U_0 + \frac{1}{2}(V - V_0)(P - P_0) = 0 \qquad (46)$$

where P is the pressure (for which we use $P^{\rm vir}$), V is the volume per atom and U is the internal energy per atom. The subscript "0" indicates the initial state (i.e. pre-shock) value.

In figure 5 we show the Hugoniot for aluminum using the equation of state from PAMD-KS, for several values of U_0, including that calculated with the AA-KS model. We take the initial temperature and density to be $T_0 = 0.025$ eV and $\rho_0 = 2.7$ g/cm^3. In principle, we could solve the PAMD-KS model under these conditions to obtain the initial energy, however, we were unable to obtain converged results for these conditions due to the presence of very long range Friedel oscillations in the pseudoatom electron densities. While the Hugoniot curve is not very sensitive to the initial pressure P_0 (since generally $P >> P_0$) it is sensitive to the initial state internal

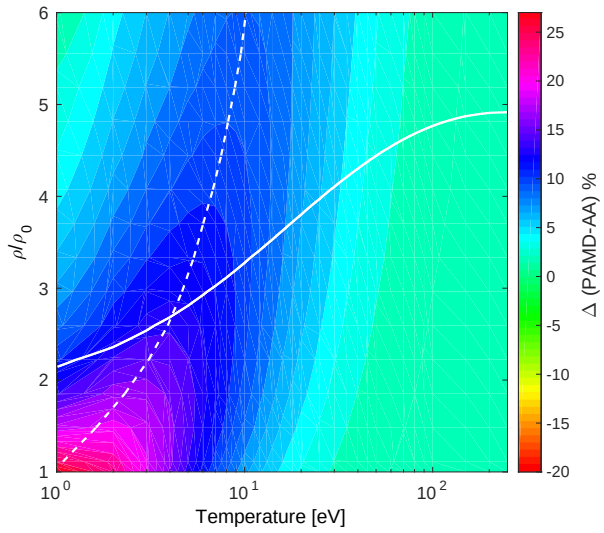

FIG. 7: Percent difference in the total pressure of aluminum calculated with the PAMD-TF and AA-TF models. The solid white line is the temperature-density path of the PAMD-TF Hugoniot. The dashed white line marks $\Gamma_{\rm eff} = 30$. The reference density is $\rho_0 = 2.7$ g/cm^3.

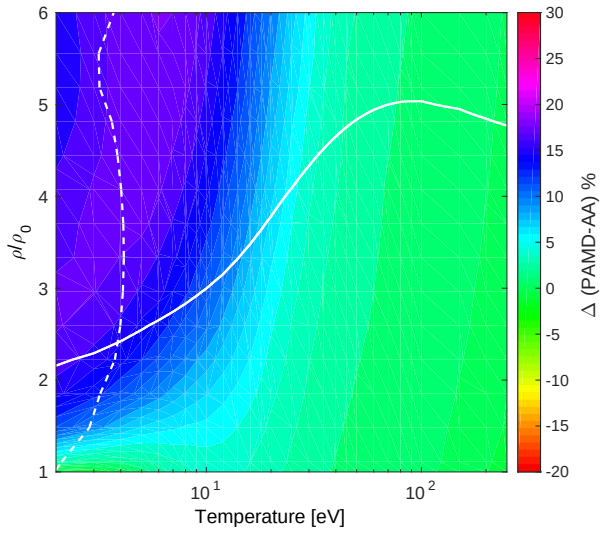

FIG. 8: Percent difference in total pressure of aluminum calculated with the PAMD-KS and AA-KS models. The solid white line is the temperature-density path of the PAMD-KS Hugoniot. The dashed white line marks $\Gamma_{\rm eff} = 30$. The reference density is $\rho_0 = 2.7$ g/cm^3 is the density of solid Al at room temperature.

energy U_0 (figure 5). For figure 6, which also shows the principal Hugoniot of Al, we have chosen the curve that best fits the experimental data of Knudson *et al.* [29] ($U_0 = -240.27\,\mathrm{E_h}$). We also show Hugoniots calculated with PAMD-TF, AA-TF and AA-KS. For these models numerical convergence was possible at the initial conditions. At the larger compression ratios (ρ/ρ_0), the data has large error bars and do not discriminate among the models (top panel of figure 6). At low compressions, the Hugoniots from the Thomas-Fermi based models are significantly softer than the data. The PAMD-KS curve also agrees with the QMD calculations of [32], better than the average atom calculation (AA-KS). However, this agreement is partly due to the fact that we have chosen U_0 for PAMD-KS to agree with the experimental data, which is reproduced very well by the QMD data. At high compression the structure in the Hugoniot curve (figures 5 and 6) due to quantum shell effects is preserved in PAMD-KS [22, 33, 34]. As an additional comparison we also show the VAAQP Hugoniot curve from ref. [22]. VAAQP is a variationally consistent Kohn-Sham average atom model. At the higher compressions it agrees very well with PAMD-KS (top panel), while at lower compressions it is somewhat softer than the data and closer to AA-KS. However, this may in part be due to the U_0 value which was calculated using VAAQP, despite those conditions being beyond the regime of validity of that model [22].

Comparison of AA to PAMD results allow us to isolate the effects of a realistic treatment of ionic structure on the principal Hugoniot. Comparing PAMD-TF to AA-TF (figure 6) we see a modest effect on the Hugoniot that remains below 10% for $\rho/\rho_0 \gtrsim 3$. In figure 7 we show a contour plot of the percentage difference in pressure predicted by the AA-TF and PAMD-TF models as a function of temperature and density. The largest differences along the Hugoniot path (solid white line) are ∼15%. In

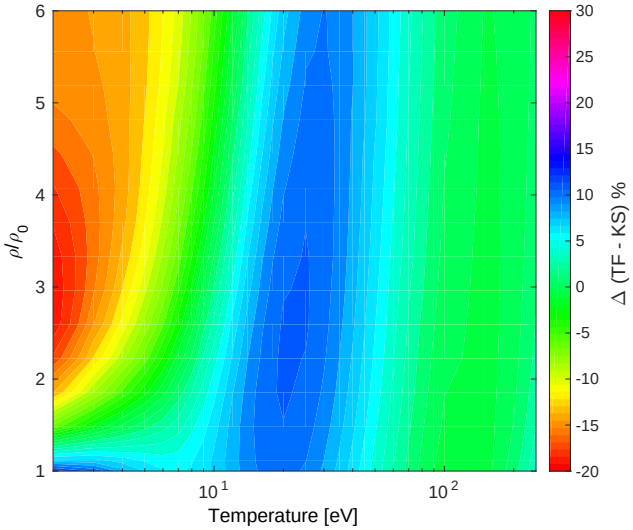

FIG. 9: Percent difference in total pressure of aluminum between the PAMD-TF and PAMD-KS. Here $\rho_0 = 2.7$ g/cm^3 is the density of solid Al at room temperature.

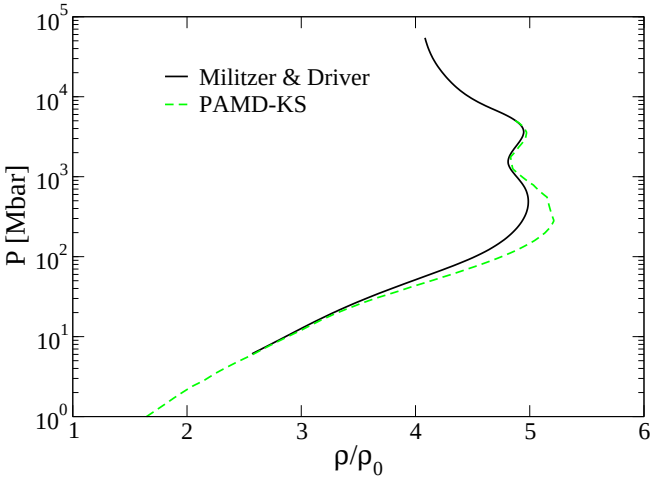

FIG. 10: Principal Hugoniot of silicon from PAMD-KS compared to the DFT-MD/PIMC results of Militzer and Driver [8]. The initial density is $\rho_0 = 2.33$ g/cm^3. Ionization of first the $2s^2 2p^6$ and second the $1s^2$ electronic shells cause the structure seen at compressions $\rho/\rho_0 > 4.5$.

general the average atom model provides a remarkably good estimate of the pressure except at low temperature and density where the difference grows to $\sim 25\%$. We find that the maximum difference between the models occurs when the effective one component plasma ion-ion coupling parameter is $\Gamma_{\rm eff} \approx 30$ [17]. The comparison between the AA and PAMD pressures along the Hugoniot for the KS calculation is quite similar (figure 8). The difference in pressure peaks at $\sim 15\%$ at low temperature and decreases steadily as the temperature rises along the Hugoniot. The $\Gamma_{\rm eff} = 30$ curve still approximates the ridge formed by the largest pressure differences.

The relative differences between the AA and PAMD pressures in figures 7 and 8 can be explained by two competing effects. The total pressure is the sum of four contributions (equation (30)), two of which (the electron kinetic $(2/3V)K_{\rm e}$ and the electrostatic $(1/3V)F^{\rm el}$) are large and of opposite sign. While they mostly cancel each other they dominate the trends seen in the figures. On the one hand, while the ionization fraction is by construction the same in PAMD and AA (but different in TF or KS) the spatial distribution of the free (screening) electrons is different. In the AA models the screening takes place entirely inside the ion sphere radius, while this is not a constraint in PAMD. In general this leads to more screening electrons being further from the nucleus in the PAMD model, resulting in a larger electron kinetic pressure, which is positive. On the other hand, strong ionic correlations (as measured by the height of the first peak of $g_{\rm ii}(r)$) correspond to a larger negative contribution to the pressure. At high temperatures the screening electrons become essentially free, which is well modeled by the average atom model, and their kinetic contribution dominates the total pressure. The net result is that at high temperature the PAMD and AA pressures are similar, at intermediate ion coupling (~ 10 eV in the figures) the PAMD pressure is larger than that of AA, and at the lowest temperatures the negative effect of increased ion correlations partially cancels the positive effect from the increased electron density further from the nuclei. At conditions corresponding to the bottom left of figures 7 and 8, the PAMD-KS $g_{\rm ii}(r)$ is more strongly peaked than that of PAMD-TF, leading to a stronger negative effect. At the top left of the figures, the situation is reversed, with $g_{\rm ii}(r)$ from PAMD-TF being more strongly peaked than that of PAMD-KS. This switch is due to the larger ionization in the TF models relative to the KS models. The ionization fraction in the KS models is relatively stable due the quantum shell effect, and remains close to 3 as we transition from the bottom left to top left of figure 8. In the TF models the ionizion fraction steadily increases from approximately 3 to 6 over the same range, leading to increased ion-ion coupling.

Figure 9 addresses the question of the accuracy of a TF EOS model compared to a KS calculation. The most striking feature is a ridge that runs almost vertically at $T \sim$ 20-30 eV where the PAMD-TF pressure can be as much as 15% higher than the PAMD-KS pressure. This is caused by the electronic shell structure in the PAMD-KS model, and is located where first the $2p$ and then the $2s$ electrons are ionizing. We find that above ~ 10 eV, the differences in pressure are caused by the differences in the electronic structure model as embodied in the TF and KS AA models. At lower temperatures new structures appear in figure 9 that generally reflect the strength of the ion coupling in the plasma, as discussed above.

For Al, ionization of the $1s^2$ electrons occurs at $T \gtrsim 300$ eV. It does not result in a large effect on the pressure but the Hugoniot shows a second turn to higher compressibility that is smaller than the one due to the $2s^2\,2p^6$ ionization (figure 5). This smaller effect is due to the large contribution from kinetic degrees of freedom at this high temperature, as well as the fact that the fractional change in the number of particles per nucleus and of the ion charge is much smaller than for the L shell ionization. We expect that the equation of state of transition metals such as Fe will show a significant feature associated with the ionization of $3d$ electrons, in addition to the $2s^2 2p^6$ feature seen in Al [34].

Since silicon is next to aluminum in the periodic table, we expect their respective EOS in the dense plasma phase to be fairly similar. This is borne out by a comparison of their principal Hugoniots that both show the same structure due to the ionization of the $n = 2$ and $n = 1$ shells, at nearly the same values of pressure and compression ratio (Figures 5 and 10). The corresponding PAMD-KS Hugoniot (Figure 10) is in generally very good agreement with the QMD/PIMC Hugoniot except around the maximum compression due to the ionization of the $2s^2 2p^6$ electrons. The PAMD-KS Hugoniot reaches a compression of 5.25 while the PIMC Hugoniot peaks at 5.0. Note that we have taken the initial state internal en-

ergy for the PAMD-KS Hugoniot be be equal to the AA-KS value (-287.16 E_h), and that the curve is not strongly affected by small changes to this value (not shown). This comparison shows for the first time that the structure in principal Hugoniots associated with the ionization of electronic shells that are a prediction of average atom models [33, 34] are also found in state-of-the-art ab initio simulations. Furthermore, the PAMD-KS model puts those features in the same pressure ranges and predict compressibilities that are close to the ab initio results. It is reasonable to expect these features to manifest themselves in experimental data once accurate Hugoniot measurements can be achieved at these extreme pressures.

III. CONCLUSIONS

The PAMD model of warm and hot dense matter has found successful applications in the calculation of pair distribution functions [11, 12], transport coefficients [13, 35], and dynamic structure factors [14]. In this contribution, we present how the equation of state can be calculated with the PAMD model, both for the Thomas-Fermi and the Kohn-Sham treatments of the electrons.

A key assumption of the PAMD model is that the total electron density is given by the linear superposition of identical, nucleus-centered electron densities. The accuracy of this approximation is reflected in the consistency between the virial and thermodynamic paths to calculate the pressure. We found that for a dense aluminum plasma, the consistency is typically $< 3\%$ over a broad range of temperatures and densities. However, the inconsistency rises rapidly at temperatures below 7 eV at low (solid) density.

We have developed a formally exact numerical trick to efficiently and accurately evaluate volume integrals of the electron density that diverge near each nucleus in the Thomas-Fermi model. This trick could also be applied in Orbital Free Molecular Dynamics simulations, allowing all-electron calculations without the need for a pseudopotential.

We have developed an approximation inspired by this numerical trick that permits the calculation of the equation of state using PAMD with a Kohn-Sham treatment of the electrons. Calculations based on this approximation were found to agree well with state-of-the-art Quantum Molecular Dynamics and Path Integral Monte Carlo simulations for beryllium, aluminum, silicon and iron. Generally, the pressures computed with the PAMD model over a wide range of elements, densities and temperatures, – both in the TF and KS versions – agree with ab initio simulations to within a few percent and rarely differ by as much as 10%.

We present the principal Hugoniot of aluminum computed with the Kohn-Sham version of PAMD up to $T = 500$ eV, which agrees well with the experimental data. As expected, structure in the Hugoniot reflects the electronic shell structure of aluminum at pressures above several tens of Mbar but the ultra-high pressure data are not accurate enough to reveal this behavior. A comparison with a Hugoniot calculated with a simple average atom model shows that the self-consistent treatment of the electronic and ionic structures has only a modest effect on the Hugoniot. The difference reaches $\sim 15\%$ on the lower part of the Hugoniot, for compression ratios $\lesssim 3$ and shrink below 5% for compression ratios > 4. The PAMD-KS principal Hugoniot of silicon is very similar to that of aluminum and can be compared to an ab initio Hugoniot up to very high temperatures. Both show the signature of the ionization of electronic shells and agree well with each other. This indicates that such features as predicted by the PAMD model (and KS average atom models as well) are not model artifacts and should be pursued experimentally.

In modeling warm and hot dense matter, ab initio molecular dynamics must switch from the Kohn-Sham to the Thomas-Fermi electron model at an intermediate temperature at the cost of neglecting shell structure at the higher temperatures. Alternatively, Path Integral Monte Carlo can be used to complement Kohn-Sham molecular dynamics, but the method is limited to low-Z elements and remains costly. A significant advantage of PAMD is that it can accurately model both warm and hot dense matter with the Kohn-Sham model of the electrons, accounting for shell structure even at keV temperatures. However, the electronic structure in Kohn-Sham PAMD is approximated by the superposition of single-center calculations. Therefore multiple scattering effects are neglected in the same way as in average atom models. The advantage of PAMD over such average atom models is an accurate accounting of the ionic disorder.

Acknowledgments

We are grateful to J. D. Kress and L. A. Collins for providing the Al and Fe QMD and OFMD data, to B. Militzer for proving the Si Hugoniot, and to O. Čertík for the high temperature TFMD data. This work was performed under the auspices of the United States Department of Energy under contract DE-AC52-06NA25396.

Appendix A: Equation of state with the average atom model

In this appendix we describe the average atom models (AA-TF and AA-KS) used for comparison to the PAMD calculations. AA-TF is the usual Thomas-Fermi-Dirac model with the $T = 0$ Dirac exchange [36–38]. The AA-KS model is essentially the same as the NWS model of [22], and has been summarized in section 2 of reference [9]. We have used the virial pressure $P^{\rm vir}$ from this model, where

$$P^{\rm vir}\, V^{\rm ion} = \frac{2}{3} K_{\rm e}^{\rm KS} + \frac{2}{3} K^{\rm I} + \frac{1}{3} F^{\rm el} + C^{\rm xc} \qquad \text{(A1)}$$

Here $V^{\rm ion}$ is the volume of the ion-sphere,

$$K_{\rm e}^{\rm KS} = \int_{V^{\rm ion}} d^3r \int_{-\infty}^{\infty} d\epsilon \, g_\epsilon \, \epsilon \, \chi(\epsilon, r) - \int_{V^{\rm ion}} d^3r \, n_{\rm e}(r) V^{\rm eff}(r) \tag{A2}$$

with

$$\chi(\epsilon, r) = \sum_{l=0}^{\infty} \frac{2(2l+1)}{4\pi} \left| \frac{y_{\epsilon,l}(r)}{r} \right|^2, \tag{A3}$$

(see appendix A of reference [12])

$$\begin{aligned} F^{\rm el} =& \frac{1}{2} \iint_{V^{\rm ion}} d^3r \, d^3r' \frac{n_{\rm e}(r) n_{\rm e}(r')}{|\boldsymbol{r} - \boldsymbol{r}'|} \\ & - \int_{V^{\rm ion}} d^3r \, \frac{Z n_{\rm e}(r)}{r}, \end{aligned} \tag{A4}$$

$$C^{\rm xc} = -F_{\rm ee}^{\rm xc} + \int_{V^{\rm ion}} d^3r \, n_{\rm e}(\boldsymbol{r}) \frac{\delta F_{\rm ee}^{\rm xc}}{\delta n_{\rm e}(\boldsymbol{r})} \tag{A5}$$

and

$$K^{\rm I} = \frac{3}{2} T. \tag{A6}$$

The internal energy per atom is

$$U = K_{\rm e}^{\rm KS} + K^{\rm I} + F^{\rm el} + U^{\rm xc}. \tag{A7}$$

where $U^{\rm xc}$ is defined in equation (28).

The average atom models thus have no knowledge of the ionic structure, the electron density is simply calculated inside a charge-neutral ion sphere with a nucleus at the origin. In contrast, in PAMD a pseudoatom is placed at each nuclear position (which are determined by molecular dynamics simulations) and the electron density is thus constructed via the superposition approximation (equation (2)).

This method of calculating the equation of state with AA-KS is qualitatively similar to the method we have used for PAMD. Thus the comparison presented in figures 7 to 9 should reflect the physical differences between the models, and not the method of calculation of the EOS.

[1] Report of ReNew workshop. *Basic research needs for high energy density laboratory physics*. U.S. Department of Energy, 2009. http://science.energy.gov/~/media/fes/pdf/workshop-reports/hedlp_brn_workshop_report_oct_2010.pdf.

[2] G. Chabrier and E. Schatzmann. *IAU Colloquium 147, The Equation of State in Astrophysics*. Cambridge, 1994.

[3] S. X. Hu, L. A. Collins, T. R. Boehly, J. D. Kress, V. N. Goncharov, and S. Skupsky. First-principles thermal conductivity of warm-dense deuterium plasmas for inertial confinement fusion applications. *Phys. Rev. E*, 89:043105, Apr 2014.

[4] L. Collins, I. Kwon, J. Kress, N. Troullier, and D. Lynch. Quantum molecular dynamics simulations of hot, dense hydrogen. *Phys. Rev. E*, 52:6202–6219, Dec 1995.

[5] Travis Sjostrom and Jérôme Daligault. Fast and accurate quantum molecular dynamics of dense plasmas across temperature regimes. *Phys. Rev. Lett.*, 113:155006, Oct 2014.

[6] G. Zérah, J. Clérouin, and E. L. Pollock. Thomas-fermi molecular-dynamics, linear screening, and mean-field theories of plasmas. *Phys. Rev. Lett.*, 69:446–449, Jul 1992.

[7] K. P. Driver and B. Militzer. All-electron path integral monte carlo simulations of warm dense matter: Application to water and carbon plasmas. *Phys. Rev. Lett*, 108:115502, 2012.

[8] Burkhard Militzer and Kevin P. Driver. Development of path integral monte carlo simulations with localized nodal surfaces for second-row elements. *Phys. Rev. Lett.*, 115:176403, Oct 2015.

[9] C. E. Starrett, J. Daligault, and D. Saumon. Pseudoatom molecular dynamics. *Phys. Rev. E*, 91:013104, Jan 2015.

[10] C. E. Starrett, D. Saumon, J. Daligault, and S. Hamel. Integral equation model for warm and hot dense mixtures. *Phys. Rev. E*, 90:033110, Sep 2014.

[11] C. E. Starrett and D. Saumon. Electronic and ionic structures of warm and hot dense matter. *Phys. Rev. E*, 87:013104, Jan 2013.

[12] C.E. Starrett and D. Saumon. A simple method for determining the ionic structure of warm dense matter. *High Energy Density Physics*, 10(0):35 – 42, 2014.

[13] J. Daligault, S. D. Baalrud, C. E. Starrett, D. Saumon, and T. Sjostrom. Ionic transport coefficients of dense plasmas without molecular dynamics. *Phys. Rev. Lett.*, 116:075002, 2016.

[14] N. M. Gill, R. A. Heinonen, C. E. Starrett, and D. Saumon. Ion-ion dynamic structure factor of warm dense mixtures. *Phys. Rev. E*, 91:063109, 2015.

[15] C. E. Starrett and D. Saumon. Models of the elastic x-ray scattering feature for warm dense matter aluminum. *Phys. Rev. E*, 92:033101, 2015.

[16] L.B. Fletcher, H.J. Lee, T. Döppner, E. Galtier, B. Nagler, P. Heimann, C. Fortmann, S. LePape, T. Ma, M. Millot, et al. Ultrabright x-ray laser scattering for dynamic warm dense matter physics. *Nature Photonics*, 9(4):274–279, 2015.

[17] T. Ott, M. Bonitz, L. G. Stanton, and M. S. Murillo. Coupling strength in coulomb and yukawa one-component plasmas. *Physics of Plasmas*, 21(11), 2014.

[18] J.-P. Hansen and I.R. McDonald. *Theory of simple liquids, Third edition*. Academic Press, 2006.

[19] D. Frenkel and B. Smit. *Understanding Molecular Simulations*. Academic Press, 2002.

[20] John C. Slater. Hellmann-feynman and virial theorems in the x-alpha method. *The Journal of Chemical Physics*,

57(6):2389–2396, 1972.

[21] M. T. Yin. Pressure and virial theorem in pseudopotential formalism. *Phys. Rev. B*, 27:7769–7771, Jun 1983.

[22] R. Piron and T. Blenski. Variational-average-atom-in-quantum-plasmas (vaaqp) code and virial theorem: Equation-of-state and shock-hugoniot calculations for warm dense al, fe, cu, and pb. *Phys. Rev. E*, 83:026403, Feb 2011.

[23] P. Hohenberg and W. Kohn. Inhomogeneous electron gas. *Phys. Rev.*, 136:B864–B871, Nov 1964.

[24] N. David Mermin. Thermal properties of the inhomogeneous electron gas. *Phys. Rev.*, 137:A1441–A1443, Mar 1965.

[25] David A. Liberman. Self-consistent field model for condensed matter. *Phys. Rev. B*, 20:4981–4989, Dec 1979.

[26] C. E. Starrett, J. Clèrouin, V. Recoules, J. D. Kress, L. A. Collins, and D. E. Hanson. Average atom transport properties for pure and mixed species in the hot and warm dense matter regimes. *Physics of Plasmas*, 19(10):102709, 2012.

[27] J. D. Kress and L. A. Collins. *Private communication*, 2012.

[28] O. Čertík. *Private communication*, 2015.

[29] M. D. Knudson, R. W. Lemke, D. B. Hayes, C. A. Hall, C. Deeney, and J. R. Asay. Near-absolute hugoniot measurements in aluminum to 500 gpa using a magnetically accelerated flyer plate technique. *Journal of Applied Physics*, 94(7):4420–4431, 2003.

[30] V.A. Simonenko, N.P. Voloshin, A.S. Vladimirov, A.P. Nagibin, V.N. Nogin, V.A. Popov, V.A. Vasilenko, and Yu. A. Shoidin. Absolute measurements of shock compressibility of aluminum at pressures p > 1 tpa. *Journal of Experimental and Theoretical Physics*, 61(4):869, 1985.

[31] A. S. Vladimirov, N. P. Voloshin, V. N. Nogin, A. V. Petrovtsev, and V. A. Simonenko. Shock compressibility of aluminum at p > 1 gbar. *JETP Lett*, 39(2):82, 1984.

[32] D.V. Minakov, P.R. Levashov, K.V. Khishchenko, and V.E. Fortov. Quantum molecular dynamics simulation of shock-wave experiments in aluminum. *Journal of Applied Physics*, 115(22):223512, 2014.

[33] B. Wilson, V. Sonnad, P. Sterne, and W. Isaacs. Purgatorio–a new implementation of the inferno algorithm. *J. Quant. Spect. Rad. Trans.*, 99:658, 2006.

[34] Balazs F. Rozsnyai, James R. Albritton, David A. Young, Vijay N. Sonnad, and DavidA. Liberman. Theory and experiment for ultrahigh pressure shock hugoniots. *Physics Letters A*, 291(45):226 – 231, 2001.

[35] D.J. Burrill, D.V. Feinblum, M.R.J. Charest, and C.E. Starrett. Comparison of electron transport calculations in warm dense matter using the ziman formula. *High Energy Density Physics*, 19:1 – 10, 2016.

[36] Paul A.M. Dirac. Note on exchange phenomena in the thomas atom. *Proceedings of the Cambridge Philosophical Society*, 26:376, 1930.

[37] R. P. Feynman, N. Metropolis, and E. Teller. Equations of state of elements based on the generalized fermi-thomas theory. *Phys. Rev.*, 75:1561–1573, May 1949.

[38] T. Blenski and B. Cichocki. Variational approach to the average-atom-in-jellium and superconfigurations-in-jellium models with all electrons treated quantum-mechanically. *High Energy Density Physics*, 3(12):34 – 47, 2007. Radiative Properties of Hot Dense Matter.